Design, fabrication, sensor fusion, and control of a micro X–Y stage media platform for probe-based storage systems

Chee Khiang Pang [a,b,*], Yi Lu [a], Chengchen Li [a,b], Jian Chen [a], Hong Zhu [a], Jiaping Yang [a], Jianqiang Mou [a], Guoxiao Guo [a], Ben M. Chen [b], Tong Heng Lee [b]

[a] A ∗ STAR Data Storage Institute, No. 5, Engineering Drive 1, Singapore 117608, Singapore
[b] Department of Electrical and Computer Engineering, National University of Singapore, 4 Engineering Drive 3, Singapore 117576, Singapore

ARTICLE INFO

ABSTRACT

Due to the renowned superparamagnetic effect encountered in conventional magnetic data storage, many alternative futuristic data storage platforms have been proposed, *e.g.* Probe-Based Storage Systems (PBSS) successfully demonstrated in the "Millipede" project [Eletheriou E, Antonakopoulos T, Binning GK, Cherubini G, Despont M, Dholakia A, et al. Millipede—a MEMS-based scanning-probe data-storage system. IEEE Trans Magn 2003;39(2):938–45]. In this paper, a micro X–Y stage with 6 mm × 6 mm recording media platform actuated by capacitive comb drives is designed and fabricated in a so-called "Nanodrive" PBSS. The developed prototype is fabricated by micromachining techniques with the integration of a 40 nm thick PolyMethyl-MethAcrylate (PMMA) recording media. Using Finite Element Analysis (FEA) on the developed platform, the first two dominant in-plane resonant modes of the micro X–Y stage at 440 Hz are captured. A displacement range of up to 20 μm can be achieved at an input driving voltage of 55 V. A Capacitive Self-Sensing Actuation (CSSA) circuit and robust decoupling control scheme are also designed for the micro X–Y stage for improved servo control.

© 2009 Published by Elsevier Ltd.

1. Introduction

Currently in 2008, many portable electronics such as digital cameras, video recorders, and cell phones, carry vast amount of consumer data and hence require high-density data storage devices with smaller sizes and form factors. However, conventional data storage devices such as magnetic hard disk drives and semiconductor memories (*e.g.* compact-flash and smart-media) have limited volumetric densities and storage capacities and are unable to keep up with the insatiable consumers' demands in today's information explosion era. But with Micro-Electrical-Mechanical-Systems (MEMS) as an up and coming technology, the development of small micro-fabricated motors and actuators to replace spinning disks in a new type of low-cost high-capacity storage device become highly feasible. A renowned example is the MEMS-actuated PBSS demonstrated by International Business Machines (IBM) in the "Millipede" project [1–4].

As such, many other researches based on similar concepts as PBSS have since sprouted, using a combination of a micro X–Y stage and a micro-probe array. In [5], Choi et al. fabricated an electromagnetic micro X–Y stage to drive the recording media, using bonding and assembling processes to fit the permanent magnets into their positions for alignments with the micro-coils. Kim et al. [6] integrated a micro X–Y stage using silicon on glass substrate with a scanning range of 50 mm and moving area of the center platform for the recording media at about 20% of the total micro X–Y stage surface area. Alfaro et al. presented a micro media actuator for positioning the recording media in X–Y directions, using silicon wafer double-side etching and wafer-to-wafer bonding processes for device fabrication in [7].

In this paper, a novel design of the micro X–Y stage with large movable media coated platform of dimensions 6 mm × 6 mm is presented for nanopositioning and control of the proposed PBSS in the so-called "Nanodrive". The proposed recording media area is about 36% of the total micro X–Y stage area. The fabrication process (including the integration of PMMA recording media) is detailed and the prototype of the device is fabricated by micromachining techniques. Extending the SSA scheme in [8], a CSSA circuit is proposed for the MEMS comb drivers in the micro X–Y stage instead of the conventional thermal sensors used in [1]

* Corresponding author. Address: Department of Electrical and Computer Engineering, National University of Singapore, 4 Engineering Drive 3, Singapore 117576, Singapore. Tel.: +65 6874 8694; fax: +65 6777 2053.

E-mail addresses: Pang_Chee_Khiang@dsi.a-star.edu.sg (C.K. Pang), Lu_Yi@dsi.a-star.edu.sg (Y. Lu), Li_Chengchen@dsi.a-star.edu.sg (C. Li), Chen_Jian@dsi.a-star.edu.sg (J. Chen), Zhu_Hong@dsi.a-star.edu.sg (H. Zhu), Yang_Jiaping@dsi.a-star.edu.sg (J. Yang), Mou_Jianqiang@dsi.a-star.edu.sg (J. Mou), Guo_Guoxiao@dsi.a-star.edu.sg (G. Guo), bmchen@nus.edu.sg (B.M. Chen), eleleeth@nus.edu.sg (T.H. Lee).

and is verified with experimental results. A robust decoupling control scheme based on open loop $\mathscr{H}_\infty$-shaping [9] is also designed to reduce mechanical crosstalk (axis coupling) in the micro X–Y stage during actuation.

The rest of the paper is organized as follows. Section 2 details the components and fundamental operation principles of the "Nanodrive". Section 3 describes the design, fabrication process, and FEA of the proposed micro X–Y stage. The CSSA for sensing the micro X–Y stage's displacement is designed in Section 4 and is verified with experimental results. Section 5 proposes a robust decoupling control method for high bandwidth and decoupled actuation of the micro X–Y stage. Finally, our conclusion and future work directions are presented in Section 6.

2. The "Nanodrive"

Currently in 2008, many universities and research institutes around the world are working on PBSS. While their approaches may differ, the main components used for high speed parallel Read/Write/Erase (R/W/E) data are similar. In this section, the proposed PBSS in the so-called "Nanodrive" is shown in Fig. 1.

In a typical PBSS, the major components include but not limited to the following:

- probes (consisting of a sharp tip on a cantilever),
- polymer storage medium,
- MEMS micro X–Y stage or MEMS scanner platform, and
- control, signal processing and sensor electronics.

The control electronics generally consist of a Digital Signal Processor (DSP) for signal processing including Position Error Signal (PES) demodulation, read channel encoding/decoding and multiplexing/demultiplexing, and control signal computations. Various controllers can take charge of Input/Output (I/O) scheduling, data distribution and reconstruction, host interface and failure management. On receiving reference commands, the micro X–Y stage is actuated to the desired locations with the help of thermal [1] or capacitive sensors [10]. Using the written in PES on the dedicated servo fields (where partitioned areas of the recording medium are specially reserved for servo data where only R operations take place, separated from user data fields where R/W/E operations are allowed to be executed), the probe tips can then perform R/W/E operations on user data field in an array operation simultaneously.
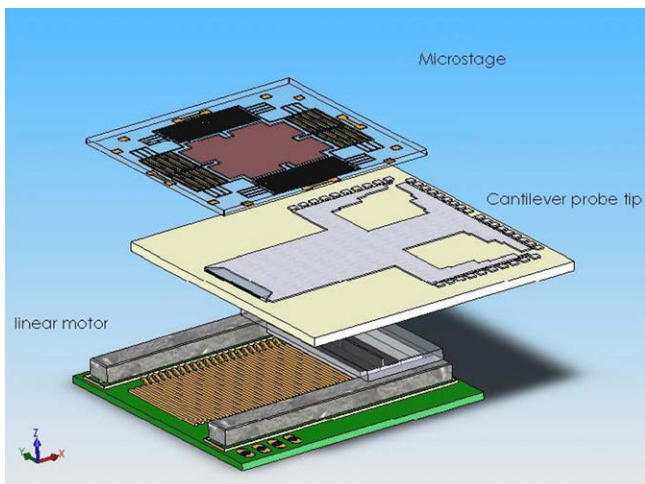
The simultaneous parallel operations of large number of probes boost the data access speed tremendously.

The nanometer wide tips of the probes perform the R/W/E operations by altering the surface physics of the polymer storage medium via either (i) thermal [1]; (ii) electric [11] or even (iii) magnetic [12] properties on a small dedicated region. The polymer storage medium is bistable and bonded on the micro X–Y stage or scanner platform during fabrication. The interference between adjacent bits must be kept to a minimal with high retention of the states after R/W/E operations to safeguard the reliability and integrity of the written-in user data. For batch fabrication, small form factor, and low-cost, it is desirable for the micro X–Y stage to be fabricated using lithography processes. The micro X–Y stage with MEMS capacitive comb driven microactuators should move the recording platform with a fast response while maintaining small mechanical crosstalk (axial coupling).

3. MEMS micro X–Y stage

In this section, the design and fabrication of the MEMS micro X–Y stage for the "Nanodrive" is detailed [13]. The layout design of the micro X–Y stage is shown in Fig. 2.

3.1. Design and simulation of micro X–Y stage

The proposed micro X–Y stage consists of a movable media platform, comb drive actuators, X and Y suspensions, springs and stationary parts. The media platform is connected to the suspensions via supporting beams, and the suspensions are connected to the anchors through the folded springs. All anchors are fixed on the Silicon-On-Insulator (SOI) substrate with which the suspensions are electrically isolated from the stationary parts. With such a suspension design, a larger media area coupled with small mechanical crosstalk (axial coupling) will be achieved [15], which are critical concerns for nano-scale bit size and spacing in high storage capacities for smaller form factor PBSS. Also, four sets of comb drive actuators are used to drive the media platform moving in X and Y directions. In each actuator, comb drive interdigital capacitance electrodes attached to the arms of the suspensions and stationary parts are used to generate electrostatic actuation.

The electrostatic driving force F is expressed by
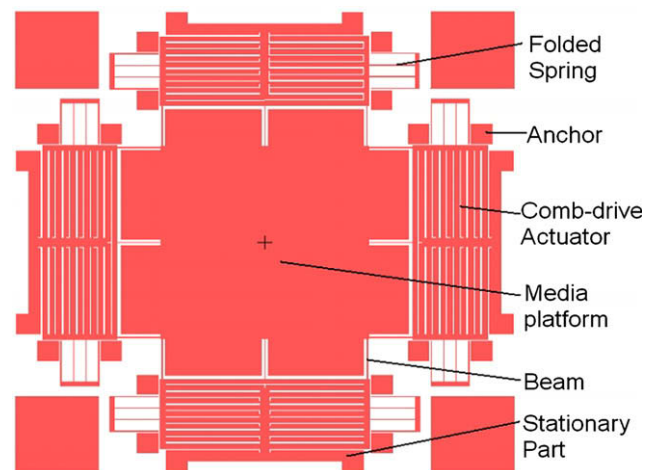
$$F = \frac{\varepsilon h n V^2}{g} \tag{1}$$

Fig. 1. Components of proposed PBSS in the so-called "Nanodrive" consisting of (i) cantilevers carrying probe tips, (ii) linear motor, and (iii) MEMS X–Y stage with recording medium.

Fig. 2. Simplified layout of a micro X–Y stage with 6×6 mm^2 recording media.

where ε is the permittivity of air, h is the height of the structure, n is the number of the electrode pairs, V is the driving voltage, and g is the gap width of the comb drive fingers. The detailed parameters of the micro X–Y stage is shown in Table 1.

3.1.1. Static

When a 55 V voltage is applied to one set of comb drive actuators, the overall electrostatic forces are calculated as 1 mN. Applying the electrostatic forces to the comb fingers for the X-axis actuation and running the static analysis in ANSYStrade, the displacement of the micro X–Y stage is determined and is shown in Fig. 3.

The displacement of the media platform achieved in the X-axis is about 20 μm. Correspondingly, the displacement in the Y-axis is 0.13 μm which is very small comparing to the comb drive gap of 3 μm. This Y-axis displacement arises from the mechanical crosstalk (axial coupling) between the X- and Y-axis from the MEMS micro X–Y stage design. Upon a step response excitation of 55 V in the X-axis, other vibratory modes are excited and hence the maximum (worst case) displacement in the Y-axis of 0.13 μm is observed.

Ideally, the Y-axis should not be excited when the X-axis is actuated. However in our proposed symmetrical structural design of the micro X–Y stage, there exists four groups of comb drives on the left, right, top, and down of the platform as shown in Fig. 2. When the platform is actuated to move in the X-axis, the spring beams of the top and down actuators will be arranged to move in a push–pull configuration. The bar supporting the spring, (*i.e.*, the top and down actuators) is not perfectly rigid, and the small deformation at that bar and the spring of top and down actuators actually caused the displacement in Y-axis of about 0.6% as the forces required for actuation are merely provided by the comb fingers at the left side only. As such, the worst-case displacement decouple ratio $\frac{y}{x}$ is 0.6% at the maximum driving voltage of 55 V.

3.1.2. Dynamic

To investigate the dynamic performance of the micro X–Y stage, modal and harmonic analysis are carried out using FEA in ANSYStrade. The first in-plane resonant mode of the micro X–Y stage at its first and second resonant frequencies of 440 Hz is shown in Fig. 4.

The frequency response of the media platform to an exciting force 1 mN in X-axis is shown in Fig. 5.

It can be seen from Fig. 5 that the micro X–Y stage exhibits a small "lumped" damping ratio and out-of-phase characteristics at the resonant frequency of 440 Hz and is perfectly symmetrical in actuator design.

3.2. Modelling of micro X–Y stage

Using the data points from FEA in ANSYStrade, the identified mathematical model $G_{xx}(s)$ in the X-axis of the MEMS micro X–Y stage from the "Nanodrive" with first in-plane resonant frequency at 440 Hz is [13]

$$G_{xx}(s) = 20\frac{(2\pi440)^2}{s^2 + 2(0.0009)2\pi440s + (2\pi440)^2} \qquad (2)$$

Table 1
Design parameters of micro X–Y stage.

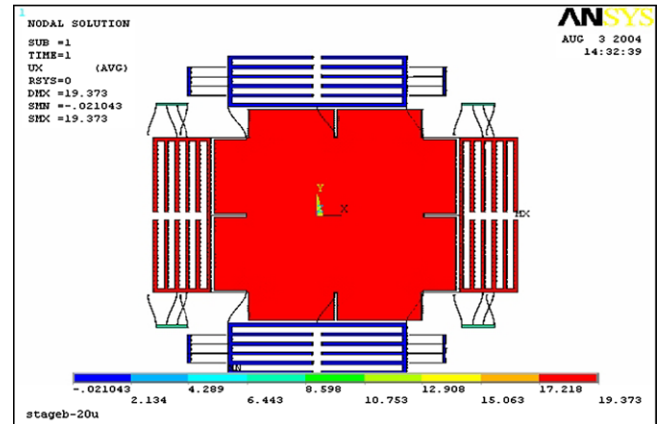| Over size	1 cm × 1 cm
Finger width	4 μm
Finger gap	3 μm
Comb-finger pairs	1920
Spring width	8 μm
Height of spring/finger	60 μm
Spring length	1 mm
Media platform	6 mm × 6 mm

Fig. 3. Displacement 20 μm of the recording media in X-axis under the driving voltage 55 V.
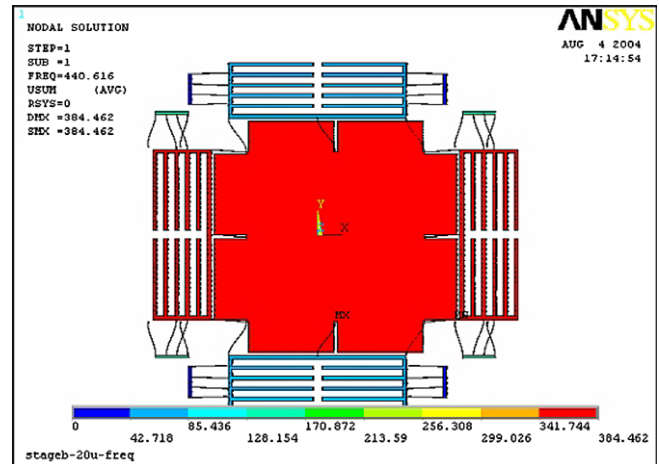

Fig. 4. The first two resonant frequencies are at 440 Hz. The mode is an in-plane sway mode.

which in essence is a second order transfer function with a very small damping ratio and no high frequency uncertainties. This property is typical of MEMS devices.

Air damping is an important factor in simulation of MEMS structures, and plays a decisive role in comb driven micro resonators especially at the high frequencies. However, it is extremely difficult to analyze the effects of the air damping with theoretical relationships, *e.g.*, using the revised Reynolds Equations with boundary conditions, slip, and gas rarefaction, considerations for air shearing damping using ANSYS alone. As such, a lumped second order Resistor–Inductor–Capacitor (RLC) electrical model or its mechanical counterpart the Mass–Spring-Damper—commonly used in system identification of MEMS structures—is proposed to include the air film in the space between the comb fingers and the substrate or structure [14] to obtain (2).

Due to the large gain at the resonant frequency, the coupling effect between the main axes cannot be ignored due the mechanical crosstalk during large span seeks. With the decoupling ratio between the main axes as 0.6%, the transfer functions of the MEMS micro X–Y stage in the Y-axis, $G_{yy}(s)$, as well as between the axes, $G_{xy}(s)$ and $G_{yx}(s)$, are

$$G_{yy}(s) = G_{xx}(s) \qquad (3)$$
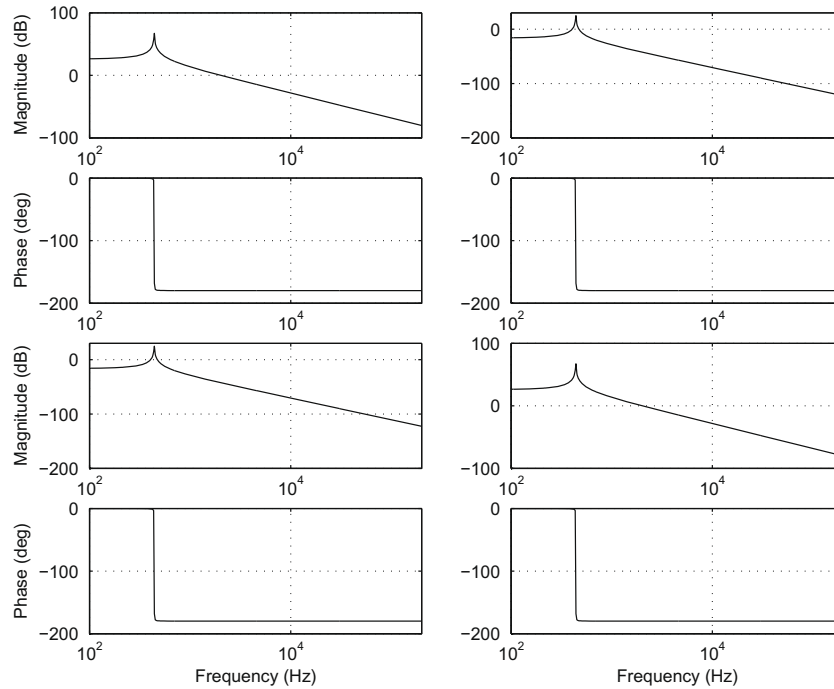$$G_{xy}(s) = G_{yx}(s) = 0.006G_{xx}(s) \qquad (4)$$

Fig. 5. Frequency response of the media platform to an exciting force 1 mN in *X*-axis.

As such, the transfer function of the MEMS micro *X–Y* stage in both axes is $G(s)$ with

$$G(s) = \begin{bmatrix} G_{xx}(s) & G_{xy}(s) \\ G_{yx}(s) & G_{yy}(s) \end{bmatrix}$$

$$= 20 \frac{(2\pi 400)^2}{s^2 + 2(0.0009)2\pi 400 s + (2\pi 400)^2} \begin{bmatrix} 1 & 0.006 \\ 0.006 & 1 \end{bmatrix} \quad (5)$$

It is worth noting that the dynamics of the micro stage in the *Z*-axis are unmodelled as the out-of-plane modes are uncontrollable. Although the existence of *Z*-axis flexible body modes affect servo-positioning performance, they occur at low frequencies which are far from the open loop gain crossover frequency to be detailed in future sections. Also, the spring constant in the *Z*-axis is much larger than that of the in-plane *X* and *Y* directions, as the beam is a high aspect ratio structure of $\frac{60}{8} = 7.5$, and constraints have been included to fix the anchors in the *Z*-axis of the platform.

3.3. Fabrication of the MEMS micro X–Y stage

In practice, MEMS-based actuators are usually fabricated from standard process including wet bulk etching, wafer bonding, surface micromachining, deep trench silicon micromachining, *etc.*, similar to standard Complementary Metal Oxide Semiconductor (CMOS) processes. By aligning the actuators in a comb drive array, nanometer positioning accuracy with the electrostatic attractive forces from the MEMS actuators can be achieved.

An integrated fabrication procedure for the micro *X–Y* stage and ultra-thin recording media layer is shown in Fig. 6. Starting from the SOI wafer, openings for releasing the large area media platform are etched until the buried oxide layer from the underside of the SOI. An ultra-thin layer of PMMA (which is commonly used as recoding media in PBSS) is formed on the topside by the spin-coat technique. The thickness of the PMMA film deposited is about 40 nm.

Next, a silicon dioxide layer is deposited by Plasma Enhanced Chemical-Vapour-Deposited (PECVD) technique. The silicon dioxide layer is patterned as both protective layer and PMMA pattern-
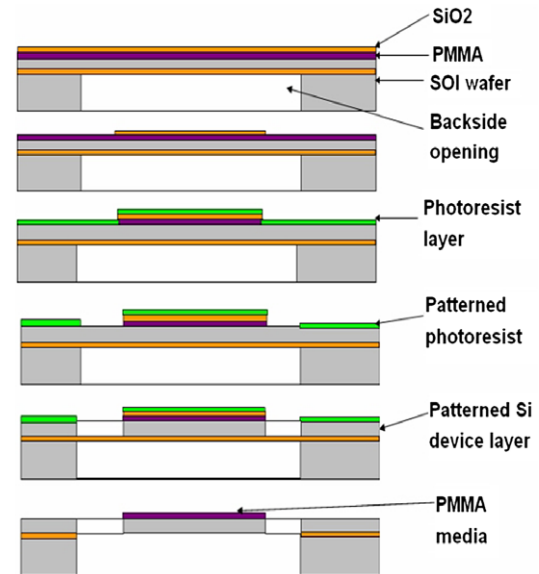

Fig. 6. Fabrication process flow.

ing mask. After PMMA patterned by oxygen plasma, a thick photoresist AZ4620 is spin-coated to cover the oxide protective layer and the patterned PMMA and is then used as a mask for *X–Y* stage etching process. The *X–Y* stage structures—including comb drives, springs, beams, and suspensions—are patterned by Deep Reactive Ion Etching (DRIE) and the photoresist is then removed by oxygen plasma. Finally, the *X–Y* stage with the moveable exposed PMMA layer platform is fully released after the silicon dioxide protective layer and SOI buried dioxide layer are removed by Buffered Oxide Etching (BOE).

The partial view of the fabricated *X–Y* stage under Scanning Electron Microscopy (SEM) is shown in Fig. 7. The large area recording media platform is released from the SOI wafer substrate
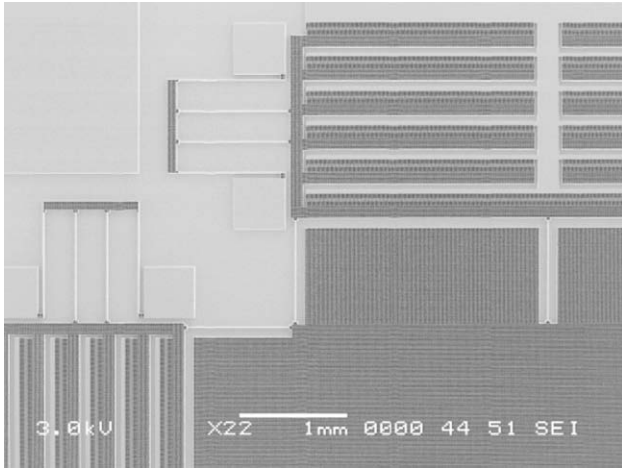
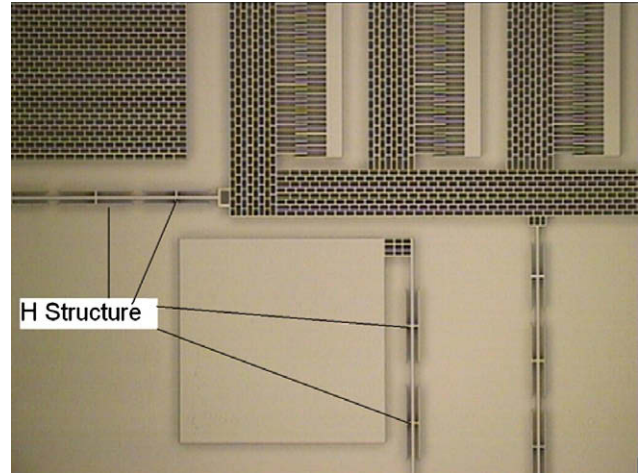**Fig. 7.** Partial view of the X–Y stage under SEM.

and is suspended by 12 supporting beams. All the movable parts are suspended by 8 pairs of folded springs.

The details of the comb drives and the suspensions are shown in Fig. 8. The finger width is 4 μm and the gap is 3 μm. The length of the finger is 75 μm, and the overlap of each pair of fingers is 30 μm.

The "H" structures are fabricated to protect the sidewall of the folded springs and supporting beams during DRIE etching since the structure-area-density of the springs and beams is lower than other areas, such as suspensions or comb drives, and is shown in Fig. 9.

The undercut of the spring width and beam width is reduced and the designed width of 8 μm is achieved.

4. Capacitive Self-Sensing Actuation (CSSA)

In this section, the design and application of sensors for the fabricated micro X–Y stage is proposed. Unlike in the "Millipede" project where probe tips are integrated and thermal sensors are used to detect the absolute position of the heated tips, a CSSA scheme shown in Fig. 10 is proposed.

4.1. Design of CSSA bridge circuit

As the actuation of the MEMS micro X–Y stage is in the in-plane direction, non-intrusive online measurements of axial displacements and velocities are not possible even upon release of the
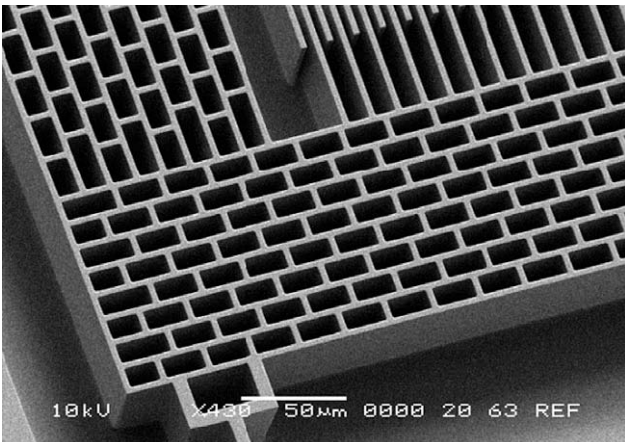

Fig. 8. Details of comb drives under SEM. Plan view of the fingers (top right).

Fig. 9. "H" structures for protecting side wall of springs during DRIE etching process.
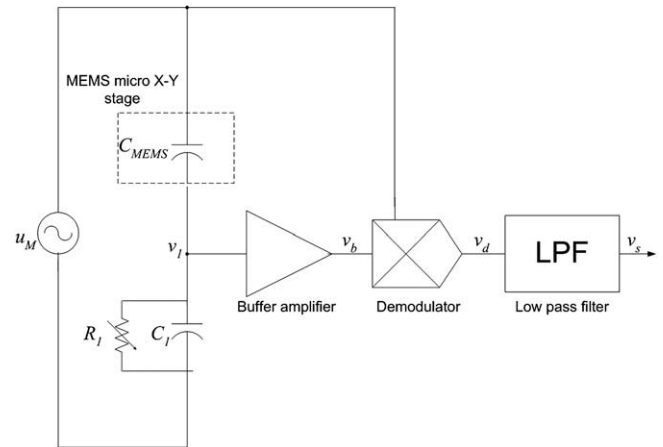

Fig. 10. MEMS-based bridge circuit for CSSA.

MEMS micro X–Y stage from the wafer. As such, offline measurements from high speed cameras coupled with image processing techniques are commonly used for frequency response measurements.

Using the fact that the capacitance C_{MEMS} of the comb drives in the MEMS micro X–Y stage is proportional to the area of overlap A

$$C_{MEMS} = \frac{\varepsilon_r \varepsilon_o A}{d} \tag{6}$$

which is in turn proportional to displacement of the MEMS micro X–Y stage for the same comb width, a CSSA bridge circuit is proposed to achieve actuation and sensor capabilities simultaneously—similar to SSA in piezoelectric actuators [8]—to decouple the capacitance information, which is linear with displacement of the MEMS micro X–Y stage.

In Fig. 10, assume that the signal generator u_M produces a sinusoid $U \sin \omega t$ of angular frequency ω rad/s. As such, the following equations hold

$$v_1 = \frac{C_{MEMS}}{C_1 + C_{MEMS}} U \sin \omega t \tag{7}$$

$$v_b = K_a v_1 \tag{8}$$

$$v_d = v_b u_M = K_a v_1 U \sin \omega t = \frac{U^2 K_a C_{MEMS}}{C_{MEMS} + C_1} \sin^2 \omega t$$

$$= \frac{U^2 K_a C_{MEMS}}{2(C_{MEMS} + C_1)} (1 - \cos 2\omega t) \tag{9}$$

where K_a is the gain of the buffer amplifier. After passing through the Low Pass Filter (LPF), the high frequency sinusoid at 2ω is demodulated and v_s can be obtained as

$$v_s = \frac{U^2 K_a C_{\text{MEMS}}}{2(C_{\text{MEMS}} + C_1)} \tag{10}$$

and hence we can interpolate C_{MEMS} to be

$$C_{\text{MEMS}} = -\frac{2v_s C_1}{2v_s - U^2 K_a} \tag{11}$$

which is proportional to the area of overlap A (hence displacement) of the MEMS micro X–Y stage in both axial directions. The above derivations exclude the effects of resistor R_1 which is commonly included to prevent drifting effects of the capacitance after prolonged operations.

The capacitance of MEMS-based devices are usually in the pico or even femto Farad region. When actuated in micro or even nanometers, the Signal-to-Noise Ratio (SNR) will be very low. As such, the modulator and demodulator in Fig. 10 are added to reduce the sensor noise level. An external sinusoidal modulator signal is essential to achieve high SNR capacitive sensing, and to actuate the MEMS micro X–Y stage for obtaining position information by artificially vibrating the MEMS micro X–Y stage at a frequency ω for capacitive self-sensing during calibration of the proposed CSSA. It should be noted that a sinusoid of frequency higher than the closed-loop bandwidth of the MEMS micro X–Y stage should be used during R/W/E operations (after calibration) to prevent vibration and excitation of the stage.

4.2. Experimental verification

For our experiments, capacitors in the pico Farad range as well as a sinusoidal modulator signal of 5 kHz are used. The demodulator, LPF of corner frequency at 10 kHz, and interpolator in (11) are implemented on a dSPACE digital control implementation system at a sampling frequency of 400 kHz. The experimental results of proposed CSSA showing linearity of output DC voltage v_{DC} and change in capacitance ΔC are shown in Fig. 11 [16] and an identified relationship of

$$v_{\text{DC}} = -0.07\Delta C - 0.11 \tag{12}$$

is obtained.

It can be seen from Fig. 11 that the output DC voltage is linear with change in capacitance which is in turn, is proportional to displacement of the MEMS micro X–Y stage. The proposed CSSA scheme calibrated with the measurements from the high speed cameras will be used for absolute displacement sensing in both axial X and Y directions.

5. Robust decoupling controller design

With the displacement sensing issue for the axial X- and Y-axes resolved, a robust decoupling controller design methodology is presented in this section. The designed digital Multi-Input-Multi-Output (MIMO) controller is evaluated with simulation results.

5.1. Choice of pre-shaping filters

To ensure robustness against parametric uncertainties in the actual micro X–Y stage during fabrication process and release, the "clean" high frequency double integrator properties of MEMS actuators is exploited. The $\mathscr{H}_\infty$-loop shaping method for MIMO controller design detailed in [9] will be modified and explored here. This one step approach is used as the open loop bandwidth (gain crossover frequency) is commonly used as a measurement of error rejection capabilities in data storage systems. Moreover, the loop shape at gain crossover frequency f_c of 4.5 kHz (about 10 times above the first in-plane sway mode of the micro X–Y stage at 440 Hz) can be improved for better gain and phase margins.

Before robust stabilization of the micro X–Y stage with normalized left coprime factorization is carried out, shaping filters $W_1(s)$ and $W_2(s)$ are cascaded before and after the micro X–Y stage $G(s)$ to shape the largest singular values into the shaped plant $G_s(s)$ as

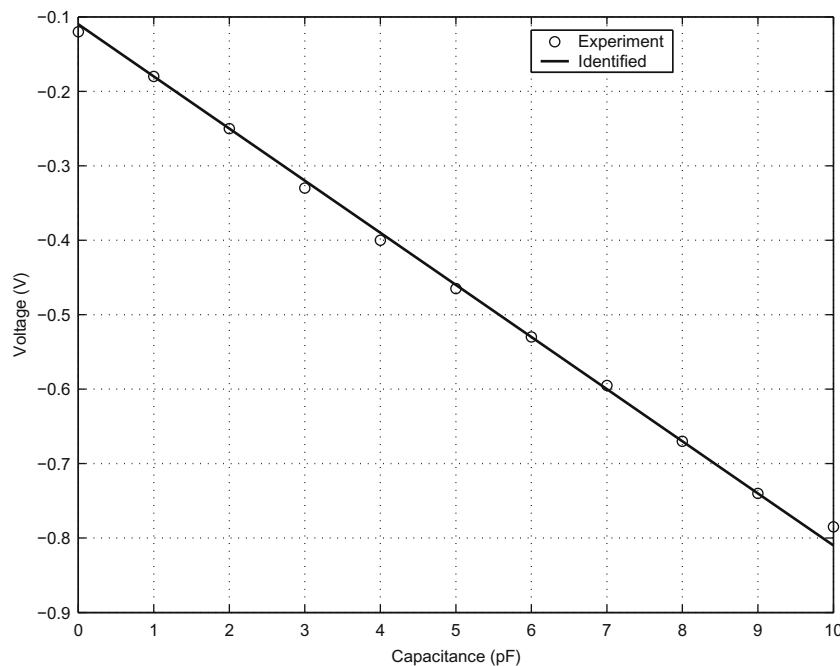$$G_s(s) = W_2(s)G(s)W_1(s) \tag{13}$$

Fig. 11. Experimental results of proposed CSSA.

For our application, $W_1(s)$ is chosen as an identity matrix to ease controller synthesis and implementation. On the other hand, $W_2(s)$ is chosen as a notch filter to compensate for the small damping ratio and large gain at the resonant frequency of 440 Hz, and a lead compensator at f_c for closed-loop stability. A decoupler is also included to further reduce the axial coupling for independent axial control. The shaping filter also prevents any numerical stability while synthesizing the robust controller and is obtained as

$$W_2(s) = \frac{s^2 + 2(0.0009)2\pi440s + (2\pi440)^2}{s^2 + 2(1)2\pi440s + (2\pi440)^2} \times K_c \frac{s + \frac{2\pi f_c}{2\alpha}}{s + 2\pi} \frac{s + \frac{2\pi f_c}{\alpha}}{s + 2\alpha2\pi f_c}$$
$$\times \begin{bmatrix} 1 & -0.006 \\ -0.006 & 1 \end{bmatrix} \tag{14}$$

where $5 < \alpha < 10$ is used typically [8]. For our simulation, we have chosen $\alpha = 6$ and by setting $|W_2(j2\pi f_c)G_{xx}(j2\pi f_c)| = 1$, K_c is tuned to ensure maximum phase lead at desired f_c. The frequency response of the shaping filter $W_2(s)$ is shown in Fig. 12.

5.2. Controller synthesis

Using the designed shaping filter $W_2(s)$, the robust stabilization controller $K(s)$ is synthesized by solving the robust stabilization problem, assuming that the shaped plant $G_s(s)$ has a normalized coprime factorization of $G_s = M_s^{-1}N_s$. It should be noted that the Laplace variable s has been omitted for simplicity in notation but without loss of generality.

Assume that the micro X–Y stage is perfectly decoupled by the decoupler in $W_2(s)$. The controller design can now be carried out independently for each axis with the diagonal and symmetrically shaped plant $G_s(s)$. With A, B, C and D as the system's dynamics state-space matrix quadruple of the micro X–Y stage's identified mathematical model shown previously in (2), the micro X–Y stage can be represented by a strictly proper system with no feedthrough (i.e. $D = 0$). As such, the controller K_x which ensures that

$$\left\| \begin{bmatrix} K_x \\ I \end{bmatrix} (I - G_{xs}K_x)^{-1} M_{xs}^{-1} \right\|_\infty \leqslant \gamma \tag{15}$$

for a specified $\gamma > \gamma^*$ where γ^* is the $\mathscr{H}_\infty$-norm of (15), is given by [9,17]

$$K_x = \begin{bmatrix} A + BF + \gamma^2(L^T)^{-1}ZC^TC & \gamma^2(L^T)^{-1}ZC^T \\ B^TX & 0 \end{bmatrix} \tag{16}$$

where G_{xs} is the shaped micro X–Y stage in the X-axis, M_{xs} is the left coprime factorization of G_{xs}, and I is the identity matrix of appropriate dimensions. F and L are then given by

$$F = -B^TX \tag{17}$$
$$L = (1 - \gamma^2)I + XZ \tag{18}$$

with Z and X being the unique positive definite solutions to the following Algebraic Riccati Equations (AREs), respectively, as

$$AZ + ZA^T - ZC^TCZ + BB^T = 0 \tag{19}$$
$$A^TX + XA - XBB^TX + C^TC = 0 \tag{20}$$

Obviously, Z and X can also be obtained by performing Schur's complements and solving with Linear Matrix Inequalities (LMI) techniques. On controller synthesis, a $\gamma^* = 1.4705$ is obtained. By choosing a $\gamma > \gamma^* = 2.0$ which results in suboptimal $\mathscr{H}_\infty$-controller, a 50% perturbation of magnitude of coprime uncertainty can be tolerated before instability. The frequency response of the synthesized $K_x(s)$ is shown in Fig. 13.

The synthesized $K_x(s)$ effectively reduces the low frequency gain and the gain crossover frequency slightly, while increases roll off at high frequencies for robust stability. The final controller $K(s)$ for the micro X–Y stage will thus be

$$K(s) = \begin{bmatrix} K_x(s) & 0 \\ 0 & K_y(s) \end{bmatrix} W_2(s) \tag{21}$$

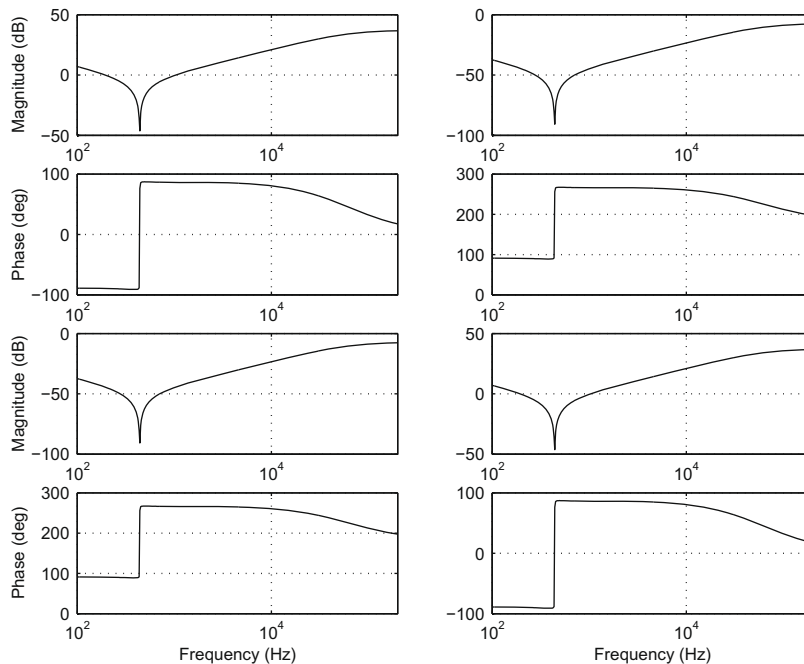and $K_y(s) = K_x(s)$ after decoupling control. The frequency response of $K(s)$ is shown in Fig. 14.

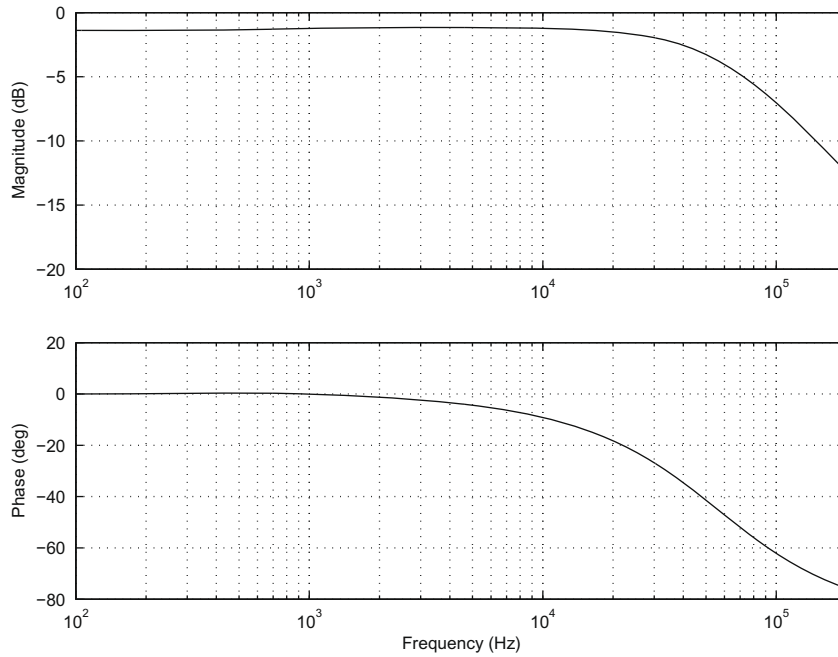**Fig. 12.** Frequency response of $W_2(s)$.
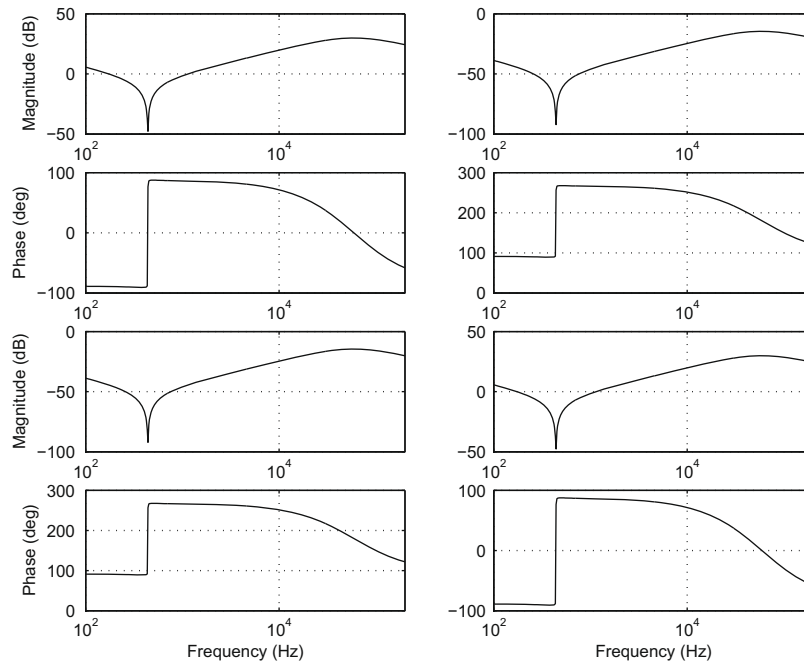
Fig. 13. Frequency response of $K_x(s)$.

Fig. 14. Frequency response of $K(s)$.

5.3. Frequency responses

The frequency responses of largest singular values in shaped plant $G_s(s)$ and open loop transfer function $K(s)G_s(s)$ are plotted in Fig. 15. It can be seen that the overall loop shape is generally unaltered, but a gentler slope is observed near the crossover frequency f_c translating into larger stability margins.

The block diagram for digital control of micro X–Y stage in both axes is shown in Fig. 16. The two-input–two-output control $K(z)$ is obtained by discretizing the $K(s)$ at sampling frequency of 400 kHz with bilinear transformation.

5.4. Time responses

For fast user data access, the overshoot of the micro X–Y stage during seek operations should be kept to a minimum. As such, a nonlinear saturator is added to $K(z)$ to ensure that the control signal does not exceed the maximum allowable voltage of 55 V. $K(z)$ must also be able to decouple the micro X–Y stage such that the interaction in the main axes is kept to a minimum. The step response of the micro X–Y stage with 20 μm for 2 ms followed by 14 μm in the X-axis (or r_x) is shown in Fig. 17. The step response of the micro X–Y stage with 14 μm at 1 ms for 2 ms followed by
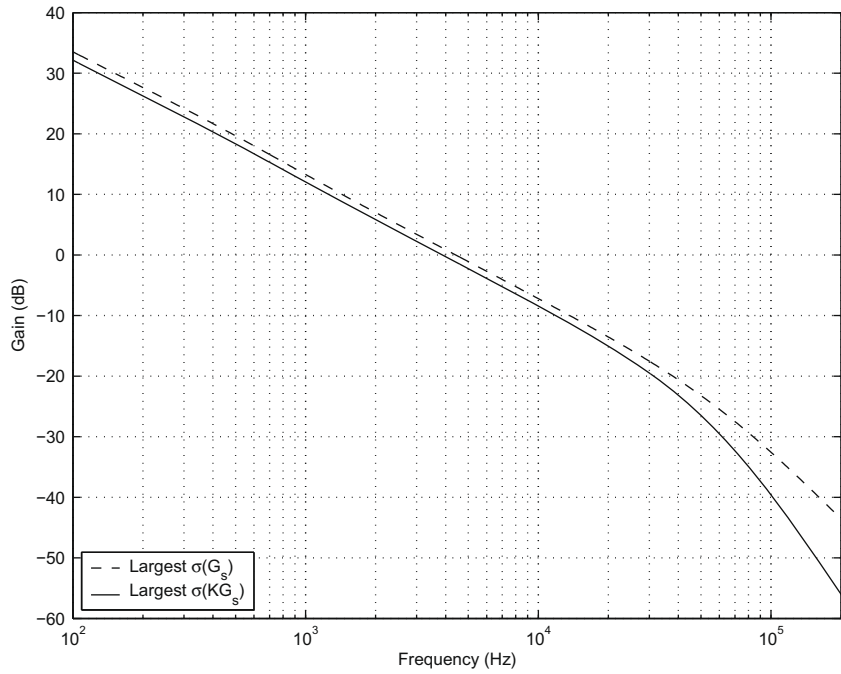
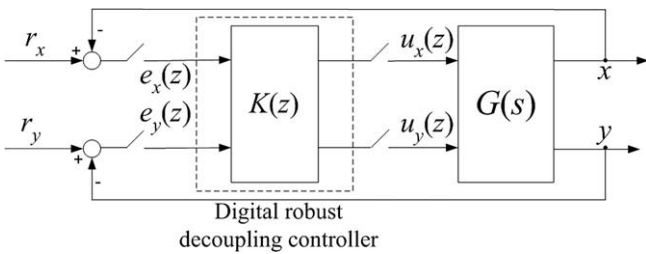**Fig. 15.** Plots of largest singular values. Dashed: $G_s(s)$. Solid: $K(s)G_s(s)$.

Fig. 16. Block diagram for digital control of micro X–Y stage.

6 μm in the Y-axis (or r_y) is shown on the same figure to observe the mechanical crosstalk of the micro X–Y stage. It can be seen that the actuation in both axes is decoupled and the interactions in both axes are in orders magnitudes of 10^{-12} m.

The corresponding control signals are shown in Fig. 18.

It can be seen from Fig. 18 that the large span seek operations with little overshoot are achieved within the control signal limitations.
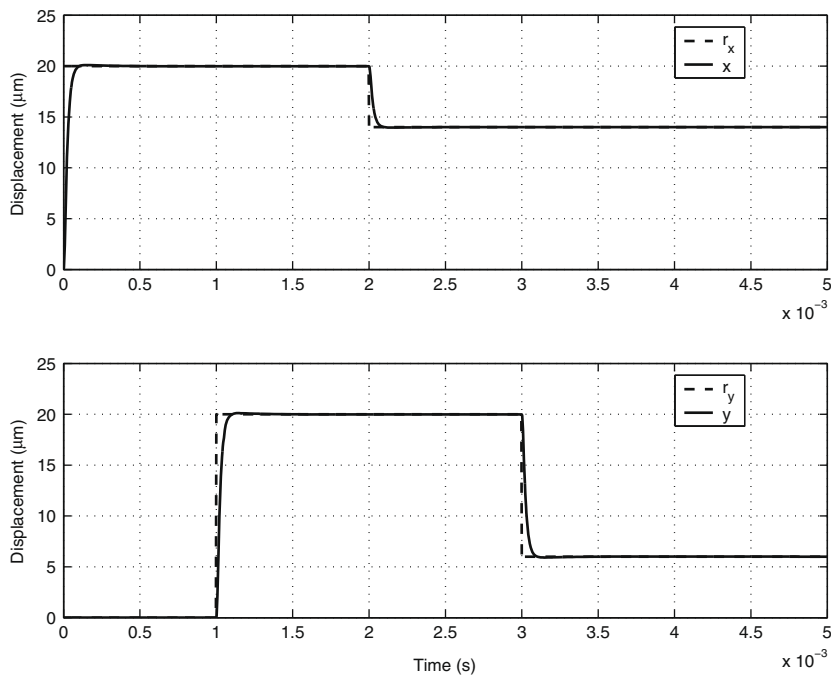

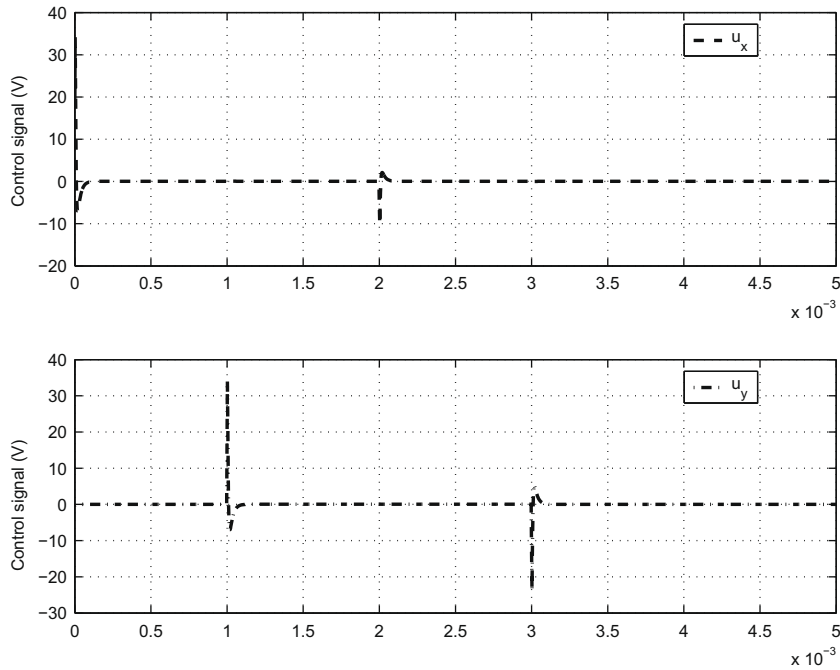**Fig. 17.** Simulated step responses.
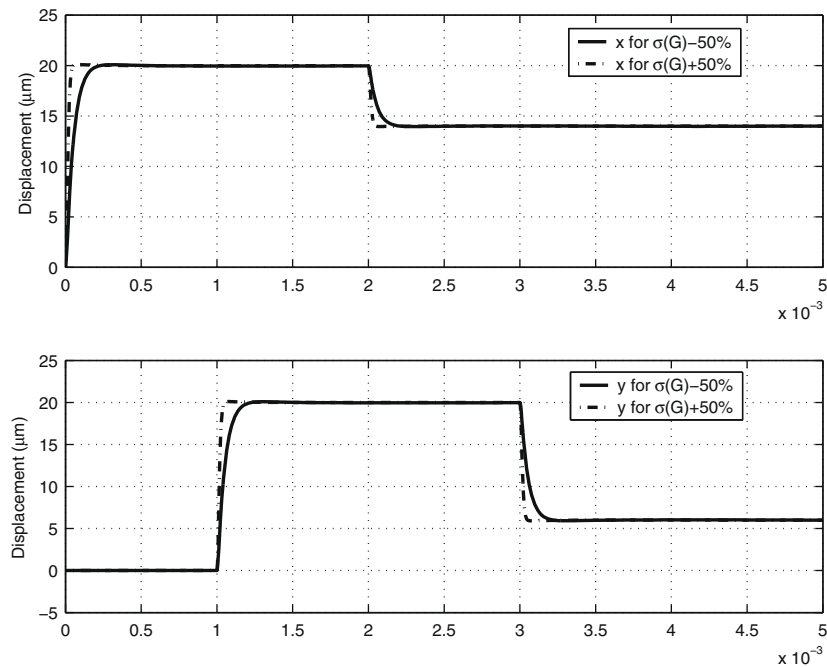
Fig. 18. Control signals.

Fig. 19. Simulated step responses for perturbed system.

5.5. Robustness analysis

Most MEMS actuators demonstrate double integrator properties at high frequencies with little uncertainties. As such, only the largest singular value of $G(s)$ is perturbed with ±50% to demonstrate the robustness of the synthesized digital controller $K(z)$. The step responses are simulated with the reference sequences r_x and r_y again and are shown in Fig. 19.

From Fig. 19, it can be seen that the closed-loop digital control system is robustly stable with the controller $K(z)$ to ±50% change in largest singular value of the MEMS micro X–Y stage.

6. Conclusion

In this paper, a novel design of the MEMS micro X–Y stage with 6 mm × 6 mm recording media platform is presented and proposed to integrate 40 nm PMMA film recording media. The displacement of the media platform is 20 μm with the driving voltage of 55 V and a Capacitive Self-Sensing Actuation (CSSA) scheme is proposed for sensor fusion, verified with experimental results. With the first two resonant in plane modes of the MEMS micro X–Y stage at 440 Hz, a robust decoupling controller scheme is proposed. Our simulation results show that the digital servo

MIMO system has strong error and vibration rejection capabilities. Following the fabrication of MEMS micro X–Y stage and development of robust decoupling control scheme with CSSA, the proposed algorithms will be tested on the MEMS micro X–Y stage with integrated recording media for R/W/E operations on the closed-loop system to obtain achievable bit and track densities for the "Nanodrive".

References

[1] Eletheriou E, Antonakopoulos T, Binning GK, Cherubini G, Despont M, Dholakia A, et al. Millipede—a MEMS-based scanning-probe data-storage system. IEEE Trans Magn 2003;39(2):938–45.

[2] Vettiger P, Despont M, Drechsler U, Dürig U, Häberle W, Lutwyche MI, et al. The "Millipede"—more than one thousand tips for future AFM data storage. IBM J Res Dev 2000;44(3):323–40.

[3] Vettiger P, Binnig GK. The Nanodrive project. Sci Am 2003;228(1):46–53.

[4] Pantazi A, Lantz MA, Cherubini G, Pozidis H, Eleftheriou E. A servomechanism for a micro-electro-mechanical-system based scanning-probe data storage device. Nanotechnology 2004;15(10):S612–21.

[5] Choi J, Park H, Kim KY, Jeon JU. Electromagnetic micro X–Y stage for probe-based data storage. J Semicond Technol Sci 2001;1(1):84–93.

[6] Kim C, Kim Y-K. Micro XY-stage using silicon on a glass substrate. J Micromech Microeng 2002;12(2):103–7.

[7] Alfaro JF, Fedder G. Actuation for probe-based mass data storage. In: Technical proceedings of the fifth international conference on modeling and simulation of microsystems; 2002. p. 202–5.

[8] Pang CK, Guo G, Chen BM, Lee TH. Self-sensing actuation for nanopositioning and active-mode damping in dual-stage HDDs. IEEE/ASME Trans Mech 2006;11(3):328–38.

[9] Glover K, McFarlane D. Robust stabilization of normalized coprime factor plant descriptions with H_∞ bounded uncertainty. IEEE Trans Automat Control 1989;34(8):821–30.

[10] Lu MS-C, Fedder GK. Position control of parallel-plate microactuators for probe-based data storage. J Microelectromech Syst 2004;13(5):759–69.

[11] Park H, Jung J, Min D-K, Kim S, Hong S, Shin H. Scanning resistive probe microscopy: imaging ferroelectric domains. Appl Phys Lett 2004;84(10): 1734–6.

[12] Carley LR, Main JA, Fedder GK, Greve DW, Guillou DF, Lu MSC, et al. Single-chip computers with microelectromechanical systems-based magnetic memory. J Appl Phys 2000;87(9):6680–5.

[13] Lu Y, Pang CK, Chen J, Zhu H, Yang JP, Mou JQ, et al. Design, fabrication and control of a micro X–Y stage with large ultra-thin film recording media platform. In: Proceedings of the 2005 IEEE/ASME international conference on AIM, MA1-04; 2005. p. 19–24.

[14] Xie M, Wang X, Yu M, Zhang M, Wang G. Analysis of the air damping in MEMS lateral driven microresonators. In: Proceedings of the ninth international IEEE CPMT symposium on high density design, packaging and microsystem integration (HDP'07); 2007. p. 1–4.

[15] Legtenberg R, Groeneveld AW, Elwenspoek M. Comb drive actuators for large displacement. J Micromech Microeng 1996;6(3):320–9.

[16] Li C. Design and implementation of position error signals for probe-based storage systems. BE thesis, National University of Singapore; 2005.

[17] Zhou K, Doyle JC. Essentials of robust control. Prentice Hall; 1997.